

Electrical Conductivity of Hydrothermally Synthesized Sodium

Lithium Magnesium Silicate

Chunxi Hai,^{a,c,*} Yuan Zhou,^{a,c,*} Masayoshi Fuji,^{b,*} Takashi Shirai,^b Xiufeng Ren,^{a,c} Jinbo Zeng,^{a,c} and Xiang Li,^{a,c}

^aKey Laboratory of Comprehensive and Highly Efficient Utilization of Sale Lake Resources, Qinghai Institute of Salt Lakes, Chinese Academy of Sciences, 18th Xinning Road, Xining 810008, China.

^bAdvanced Ceramics Research Center, Nagoya Institute of Technology, Honmachi 3-101-1, Tajimi, Gifu 507-0033, Japan.

^cKey Laboratory of Salt Lake Resources Chemistry of Qinghai Province.

*Corresponding Authors. E-mails: haicx@isl.ac.cn, zhouy@isl.ac.cn

Abstract

This study is focused on the investigation of the electrical conductivity of sodium lithium magnesium silicate (Na hectorite) dispersion, which was hydrothermally synthesized from the brine of the Qarhan Salt Lake. Depending on the duration of the utilized hydrothermal treatment procedure, porous hectorite samples with tunable aspect ratios ranging from 70 to 500 were produced from the delaminated specimens stacked along the *c*-axis. More, benefiting from the appearance and enlarged size of these stacked layers, the as-prepared Na hectorites obtained at 180°C for longer than 96 h own the average conductivities in excess of $\times 10^{-4}$ S·cm⁻¹ when the concentrations are higher than 1.25 mg·mL⁻¹, which is largely influenced by their size, crystallinity and aspect ratio.

Keywords: A. nanostructures, B. crystal growth, C. X-ray diffraction, D. ionic conductivity

1. Introduction

Owing to its uniquely layered structure, good mechanical property, high ion exchange capacity, and the presence of charged layers in the octahedral lattice induced via isomorphic substitution, lithium magnesium silicate (hectorite), which represents 2:1 layered smectite clay, has been commonly used during recent decades as a single ion conductor as well as in photoenergy and photocatalysis applications [1-6]. Hence, Li hectorites with the cross-connected three-dimensional superstructure exhibit enhanced ionic conductivity in poly (ethylene oxide) electrolyte, which exceeds 10^{-4} S·cm⁻¹ at ambient temperature [1-4]. Moreover, due to the defect-induced spatial separation of electron (e⁻) and hole (h[•]) carriers in semiconductors, porous hectorites with different interlayer cations (such as Na⁺, K⁺, and Li⁺ ones) are considered highly efficient charge-separated state stabilizers for photo-devices [5]. Furthermore, it has been reported that the formation of various disperse superstructures of clay nanolayers with different sizes, shapes, and physical properties plays an important role in improving the optical properties of different colloidal semiconductors such as CdS/halloysite, TiO₂/bentonite, and Bi₂WO₆/rectorite [5-7]. However, due to their high surface energy, nanolayers with low aspect ratios tend to become aggregated through the “face-to-face”, “edge-to-edge”, or “edge-to-face” interactions, which deteriorate many of their characteristics such as high resistance to aggregation, porosity, and electrical conductivity [8]. Therefore, increasing the aspect ratio of layered nano-materials without changing their structure is the prerequisite for the successful development of superstructures [9].

Currently, exfoliation techniques are widely employed for improving the aspect ratios of nanolayered materials (including MoS₂, MnO₂, Mg₆Al₂(OH)₁₆, tactoid clays, and hectorites); however, they are accompanied by the inevitable breakage of the treated structure [10-13]. Owing to the complexity and uncontrollability of the exfoliation procedure utilized for natural or synthetic hectorites, various researchers attempted to develop hectorites with tunable properties [8,12-14]. For example, Kalo et al. have reported the synthesis of Li hectorites with very large aspect ratios (>10,000) through a solid-state reaction conducted at a temperature of 1350°C using MgCO₃·Mg(OH)₂·xH₂O as a starting material [12]. The group of Vicente and Sánchez published several papers on the synthesis of Li⁺/Na⁺ hectorites with high specific surface areas (SSAs) of up to 603 m²·g⁻¹ via a microwave-assisted method [8,14]. Moreover, in recent decades, numerous studies focused on the hydrothermal crystallization of hectorites [15-18] in the presence of water-soluble organic compounds (tetraethylammonium (TEA)) or polymers (such as poly(ethylene oxide) and poly(vinylpyrrolidone)) have been reported. Unfortunately, in addition to the necessity of removing organic additives, the lateral dimension of the as-obtained synthetic hectorites did not exceed 300 nm. Furthermore, the utilization of freshly prepared brucite (Mg(OH)₂) reagent and minimum duration of the hydrothermal reaction represent the two key parameters for the synthesis of hectorites with high crystallinity and aspect ratios [14-20].

Qarhan Salt Lake, which is located in the Qinghai Province of China, is rich in Li, Mg, Na, and K elements. In particular, it contains about 4800 million tons of

magnesium salts. Consequently, finding a suitable application for the Mg-rich salt lake brine containing Li elements is very important for the effective use of salt lake resources in China.

In this paper, we report the synthesis of Na hectorites with high aspect ratios from the Mg-rich brine of the Qarhan Salt Lake, which was utilized as a source of both Mg and Li elements. For large-scale potential applications, the relationship between the electrical conductivity and physico-chemical properties of the as-synthesized Na hectorites dispersions has been investigated in detail.

2. Experimental

2.1 Chemicals

In this study, the concentrated Qarhan Salt Lake brine containing $0.91 \text{ mol}\cdot\text{L}^{-1}$ of lithium, $4.55 \text{ mol}\cdot\text{L}^{-1}$ of magnesium, $0.07 \text{ mol}\cdot\text{L}^{-1}$ of sodium, $0.17 \text{ mol}\cdot\text{L}^{-1}$ of potassium, and $0.24 \text{ mol}\cdot\text{L}^{-1}$ of boron was utilized. In addition, $\text{NH}_3\cdot\text{H}_2\text{O}$ (28 wt% solution), analytical grade $\text{Na}_2\text{SiO}_3\cdot 9\text{H}_2\text{O}$, tris(ethylenediamine)cobalt(III) chloride ($\text{C}_6\text{H}_{24}\text{Cl}_3\text{CoN}_6\cdot 3\text{H}_2\text{O}$), and HF (40 wt% solution) were purchased from Sinopharm Chemical Regent Co., Ltd. All reagents were used as received without further purification. A 9 M $\text{NH}_3\cdot\text{H}_2\text{O}$ solution was prepared by diluting the 28% $\text{NH}_3\cdot\text{H}_2\text{O}$ solution with a proper amount of deionized water.

2.2 Synthesis of hectorites

First, 50 mL of the as-received concentrated salt lake brine was diluted with 50 mL

of deionized water followed by the precipitation with 3 mL of 9 M $\text{NH}_3 \cdot \text{H}_2\text{O}$ solution at a temperature of 50°C in a water bath for 1 h. After thoroughly washing with deionized water to the neutral pH, white precipitate (denoted as a precursor) was obtained.

The freshly prepared wet precursor was directly mixed with 11.69 g of $\text{Na}_2\text{SiO}_3 \cdot 9\text{H}_2\text{O}$ in 138.3 mL of deionized water to satisfy the stoichiometric composition of hectorites [8,12,16-18]. The obtained mixture was heated to 180°C for 8, 15, 24, 48, 72, 96, 120, 192, or 264 h inside a 150-mL stainless autoclave reactor (the resulting samples were denoted as Hec-x h, where x indicated the hydrothermal reaction time). Due to the hydrolysis of Na_2SiO_3 in aqueous solution, the pH of the as-prepared mixture before hydrothermal treatment was around 12.4 (without adding any acid-base pH adjusters).

2.3 Electrical conductivity and pH measurements

Na hectorite aqueous suspensions were prepared by mixing the 0.0135, 0.0270, 0.0540, 0.0810, 0.1080, 0.1350, 0.1620, 0.1890, 0.2160 and 0.2700 g pre-dried samples with 90 ml of deionized water ($18.25 \text{ M}\Omega \cdot \text{cm}$) in an ultrasonic bath 25°C for 10 min followed by the rigorous magnetic stirring for 240 min to obtain homogeneously dispersed suspensions, respectively. The concentrations of as-prepared suspensions were 0.15, 0.30, 0.60, 0.90, 1.20, 1.50, 1.80, 2.10, 2.40 and $3.00 \text{ mg}\cdot\text{mL}^{-1}$, respectively. Electrical conductivities and pH variations of the as-prepared hectorite suspensions were measured at different concentrations with a

Senven Excellence multi-meter (Mettler-Toledo International Trading Co. Ltd.) equipped with a quality pH meter (InLab Science Pro-ISM) and an electrical conductivity meter (InLab 710). All measurements were performed at a temperature of $20\pm 1^\circ\text{C}$. In order to eliminate the influence of the dissolved CO_2 from air during the preparation stage, all suspensions were sealed with parafilm. In addition, deionized water was used as a blank sample for comparison purposes.

2.4 Characterization

Powder X-ray diffraction (PXRD) patterns of the as-prepared samples were obtained using a Rigaku D/Max-2200 PC diffractometer with $\text{Cu K}\alpha$ radiation ($\lambda = 0.15418 \text{ nm}$). The X-ray tube was operated at 40 kV and 30 mA. The data were collected with an angular step of 0.05° at 2 s per step and sample rotation.

Chemical analysis of the as-synthesized samples was conducted via inductively coupled plasma atomic emission spectroscopy (ICP–AES, Thermo ICAP6500) by dissolving 4 mg of the samples in 0.5 mL of HF (40 wt%) followed by the dilution with distilled water to a fixed volume (50 mL). Cation exchange capacity (CEC) was determined by dispersing 0.02 g of the pre-dried synthetic hectorites at 100°C in 20 mL of 0.0005 M tris(ethylenediamine)cobalt(III) chloride ($\text{C}_6\text{H}_{24}\text{Cl}_3\text{CoN}_6\cdot 3\text{H}_2\text{O}$) aqueous solution with the subsequent magnetic stirring at a temperature of 25°C for 10 h and centrifugation. The obtained supernatant was analyzed by ICP–AES.

Solid-state nuclear magnetic resonance (NMR) experiments were conducted on a Bruker Avance 400 spectrometer equipped with a 4-mm probe and operated at a

frequency of 79.51 MHz for ^{29}Si . ^{29}Si MAS (Magic Angle Spinning) spectra were recorded under high-power proton decoupling conditions.

Specimen imaging was conducted using a field-emission scanning electron microscope (FE-SEM, Su8010, Hitachi, Japan) and a high-resolution transmission electron microscope (HR-TEM, Tecnai G2TF20, FEI Corp. USA) equipped with a selected area electron diffraction (SAED) module.

Nitrogen adsorption and desorption isotherms were recorded on Quantachrome Instruments Autosorb IQ2. Prior to analysis, the samples were outgassed at a temperature of 150°C for 4.2 h. SSA and pore size distribution were determined using the Brunauer-Emmett-Teller (BET) and Barrett-Joyner-Halenda (BJH) methods, respectively.

An ultraviolet-visible (UV-vis)/near infrared (NIR) spectrometer (PE 750) was used to obtain diffuse reflectance spectra (DRS). Surface characteristics of the studied samples were evaluated via Fourier transform infrared spectroscopy (FT-IR, Thermo-Nicolet Nexus, USA) in the spectral range of 400–4000 cm^{-1} at a resolution of 4 cm^{-1} . Each sample was mixed with the oven-dried spectroscopic grade KBr and pressed into an almost transparent disc.

Thermal properties of the samples dried at 80°C for 12 h in a vacuum oven were evaluated using a computer-controlled thermogravimetric/differential thermal analysis instrument (TG/DTA, SDTQ600, USA). The corresponding measurements were performed between the room temperature and 1100°C at a heating rate of 5°C/min.

3. Results and discussion

3.1 Physico-chemical properties of synthetic Na hectorites

Fig. 1 displays the XRD pattern of the precursor precipitated via the dropwise addition of 9 M $\text{NH}_3 \cdot \text{H}_2\text{O}$ to the salt lake brine. The major reflections observed at $2\theta = 18.8^\circ, 33.3^\circ, 37.6^\circ, 50.7^\circ, 58.9^\circ,$ and 72.1° corresponded to the (001), (100), (101), (102), (110), and (201)

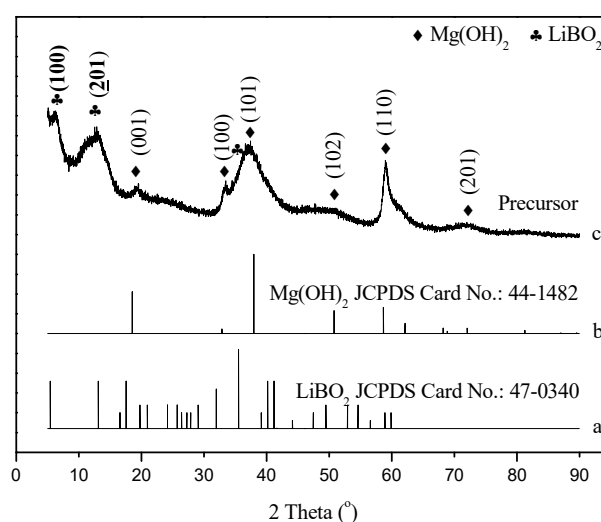


Fig. 1. An XRD pattern obtained for the precipitated precursor.

crystal planes of hexagonal $\text{Mg}(\text{OH})_2$, which was in good agreement with the standard JCPDS card (No. 44–1482) [21]. While the reflections at $2\theta = 5.8^\circ$ and 13.1° can be identified as the (100) and (201) planes of LiBO_2 (JCPDS card No. 47–0340), the broadened peak at $2\theta = 37.6^\circ$ is attributed to the overlapping (101) and (022) planes of $\text{Mg}(\text{OH})_2$ and LiBO_2 , respectively. The obtained results indicate that the main component of the precipitated precursor is $\text{Mg}(\text{OH})_2$ with a small amount of LiBO_2 impurity.

After heating the prepared samples to 180°C for different periods, the aqueous mixtures of Mg(OH)₂ precursor and Na₂SiO₃·9H₂O were fully converted to hectorite-like powders, as indicated by the XRD patterns depicted in Fig. 2. The reflections at around 2θ = 19.4°, 33.7°, and 60.18° are assigned to the (110/020),

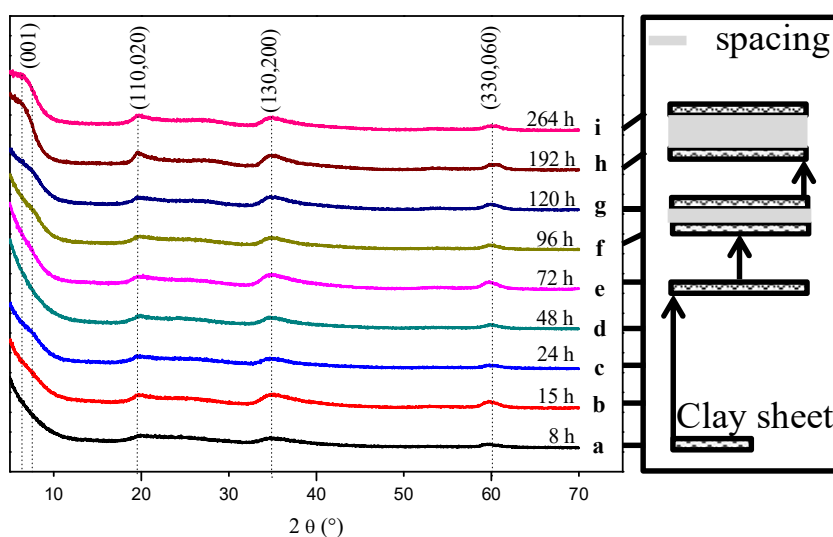


Fig. 2. XRD patterns obtained after heating the as-synthesized samples to 180°C for (a) 8 h, (b) 15 h, (c) 24 h, (d) 48 h, (e) 72 h, (f) 96 h, (g) 120 h, (h) 192 h, and (i) 264 h.

(130/200), and (330/060) planes of hectorites, respectively [16-18]. No characteristic peaks of any impurities (such as Mg(OH)₂ and LiBO₂) were detected for all patterns, indicating that not only a highly pure hectorite-like material was synthesized from the salt lake brine, but also that LiBO₂ impurity had no apparent effect on the crystal structure of synthetic hectorites. The greater is the hydrothermal reaction time, the higher are the intensities of these typical diffraction peaks, which confirm the preferred growth of the as-prepared hectorite-like material across the (*ab*) plane. In addition, it should be noted that the main difference between the synthetic hectorites

hydrothermally synthesized at 180°C for less (patterns a–e in Fig. 2) and more than 96 h (patterns f–i in Fig. 2) is the shape of their (001) reflection, which indicates whether the structure of the formed material is stacked [22]. In particular, the low-angle shift of the (001) reflection peak from $2\theta = 7.83^\circ$ (for Hec-96 h and

Table 1. Compositions, SSAs, and pore sizes of the as-synthesized hectorites after heating to 180°C for different times.

Sample	SiO ₂ (ppm)	Mg (ppm)	Li (ppm)	Na (ppm)	Si/Mg (mol/mol)	CEC (mEq/g sample)	BET S.A. (m ² /g)	Pore Size (nm)
Hec-8h	38.74	14.45	0.29	0.95	1.07	0.33	559	1.7
Hec-15h	36.13	13.89	0.35	1.18	1.04	0.34	519	1.7
Hec-24h	39.17	13.61	0.27	0.88	1.15	0.35	523	1.7
Hec-48h	39.24	13.61	0.26	0.86	1.15	0.39	546	1.7
Hec-72h	41.54	13.05	0.56	1.86	1.27	0.41	520	1.7
Hec-96h	40.40	12.91	0.61	2.01	1.25	0.45	510	1.7
Hec-120h	39.99	12.77	0.67	2.21	1.25	0.45	391	1.7
Hec-192h	40.00	11.79	0.66	2.19	1.37	0.47	389	1.7
Hec-264h	42.00	11.79	0.74	2.44	1.42	0.48	314	1.7

Hec-120 h) to 6.26° (for Hec-192 h and Hec-264 h) observed in this study indicates the formation of a layered structure with a broadened interlayer distance. The calculated basal spacing of Hec-192 h and Hec-264 h (1.409 nm) is slightly higher than that of Hec-96 h and Hec-120h (1.127 nm). Furthermore, because the lattice

parameter of one hectorite clay unit is around 0.96 nm [19], the gallery region of the as-synthesized hectorites has a length of 0.167–0.449 nm, which is due to the presence of interlayer cations such as Li^+ , K^+ , and Na^+ ones [12,14,19]. Since very little pattern differences exist between synthetic hectorites with various cations [16-18], it was impossible to obtain any specific information about particular types of the interlayer cations in the prepared samples from their diffraction patterns.

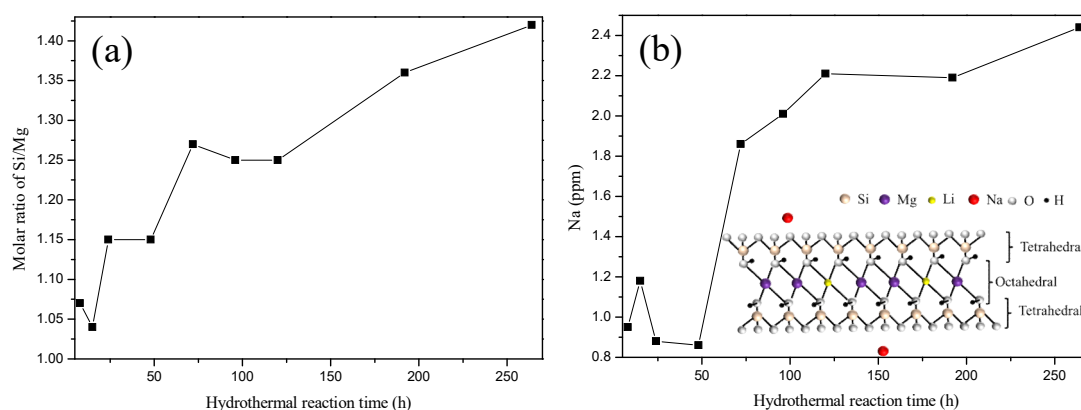


Fig. 3. Variations of the (a) molar ratio of Si/Mg and (b) Na content in synthetic hectorites plotted as functions of the synthesis time.

Table 1 lists the composition analysis results for the as-synthesized hectorites, which show that the only type of interlayer cations corresponds to Na ions with a radius of r_{Na^+} 0.102 nm; hence, the produced samples can be described as Na hectorites. Despite the large contents of K, Na, and Li ions in the as-obtained brine, the presence of only Na cations in the as-synthesized hectorites indicates their greater ability to be intercalated into the hectorite lattice (as compared to those of K (r_{K^+} is 0.122 nm) and Li (r_{Li^+} is 0.076 nm) ions). Moreover, as shown in Table 1 and Fig. 3, the molar ratio of Si/Mg, Na content, and CEC of the produced material increase with

an increase in the hydrothermal treatment time. Thus, the Si/Mg molar ratio increased from 1.04 to 1.42 with synthesis time, which was very close to the ideal molar ratio of 1.5 obtained for hectorites [16-18], which suggested the condensation of silicates in the bone structure of the as-synthesized materials [18].

The chemical bonding environment of SiO₄ tetrahedra in the as-prepared samples was evaluated by recording their ²⁹Si-MAS-NMR spectra (see Fig. 4(a)). They show that the analyzed specimens exhibit two broad resonance peaks at -85.1~-88.3 ppm and -93.9~-95.5 ppm, which can be identified as the Q2 and Q3 silica species, respectively (here, the terms Q and x in Q_x (x=2, 3) denote the Si atom bonded to four oxygen atoms and number of Si neighbors, respectively [19]). The relatively high widths of these two peaks can be attributed to the chemical and structural complex of silicon nuclei in the sample framework. According to Fig. 4(b), which shows the top view of the hectorite crystal structure, two different chemical environments exist for Si atoms: Q3 units arranged in honeycomb hexameric rings and Q2 units located at the sheet edges. In our study, prolonging the hydrothermal synthesis time from 8 to 264 h shifts the silicate Q3 Si(OSi)₃(OMg) peak from -95.5 ppm to -93.9 ppm, which is eventually stabilized at around -94.0 ppm after 24 h. This Q3 peak appears between -95.0 and -94.0 ppm for natural hectorites [16,22-23], at -100 ppm for metakaolinite bricks, at -97.0 ppm for talcs, at -95.0 ppm for Li hectorites, and at -94.0 ppm for montmorillonite [19,24-26]. Another peak centered at -85.0 ppm confirms the presence of silicon species with the Si(OSi)₂(OM)₂ (M=H, Mg) structure. The chemical shift of Si(OSi)₂(OH)₂ on the MCM-41 silica surface was observed at

–89.00 ppm [27,28], while the chemical shift of $\text{Si}(\text{OMg})(\text{OSi})_2(\text{OH})$ for the layered talc with the ideal formula $\text{Mg}_3\text{Si}_4\text{O}_{10}(\text{OH})_2$ was detected at –85.20 and –87.50 ppm [19]. However, it was very difficult to identify the Q2 species in the present study via ^{29}Si -MAS-NMR spectroscopy. In addition, it should be noticed that at treatment times greater than 24 h, the two characteristic Si bands exhibit a low-field shift of about 2 ppm, which results from the intensification of the Si–O–Mg band between the tetrahedral and octahedral sheets [29,30] and indicates the improved structure identity of tetrahedral silicon sheets in the as-prepared samples.

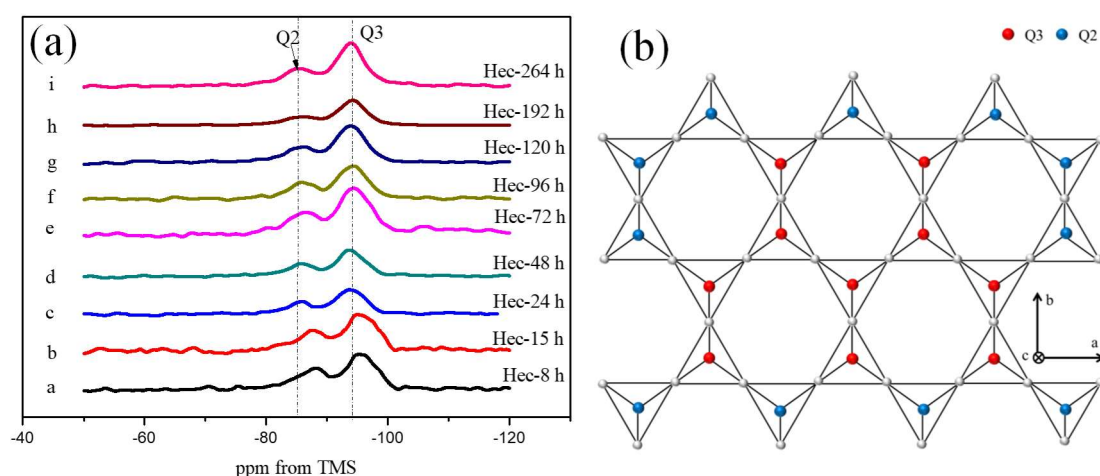


Fig. 4. (a) Solid-state ^{29}Si -MAS-NMR spectra of the hectorite clays hydrothermally treated at a temperature of 180°C for different periods. (b) A schematic of the silicate tetrahedral sheet (top view). Different colors represent various chemical bonding structures of the silicate lattice.

Fig. 5(a) shows the FT-IR spectra of the Hec-8 h, Hec-120 h, and Hec-264 h samples. Because the peaks centered at 3430 and 1630 cm^{-1} correspond to the physically absorbed water [31], the spectral region from 1200 to 4000 cm^{-1} is not displayed here. As shown in Fig. 5(b), due to the interactions between the interlayer water species and

the clay lattice, both the H–O and Si–O band vibrations largely depend on the chemical environment of the Si and O atoms. Briefly, the (a) H–O \cdots H(H₂O_{inter}), (b) H–O \cdots H(H₂O_{between}), (c) H–O–Si, and (d) H–O–Mg OH groups can exist in nanolayered clays. Furthermore, because the Si–O stretching vibrations in the layered

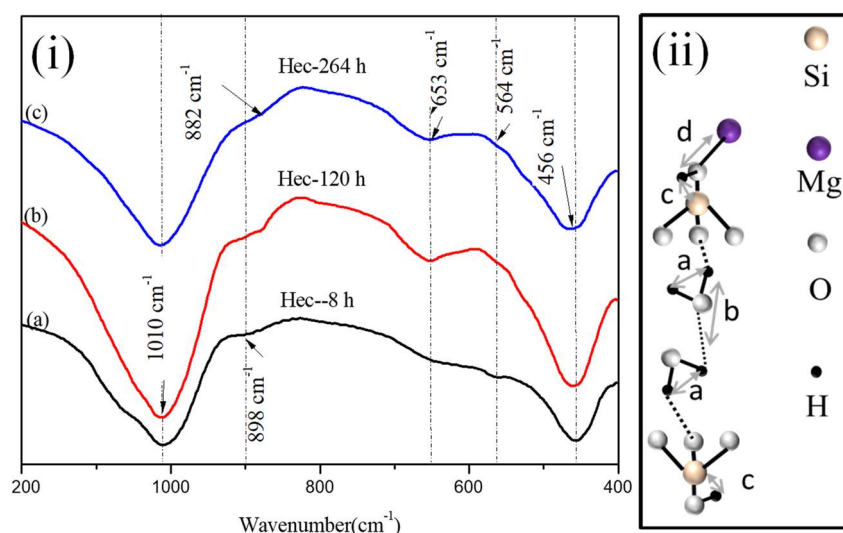


Fig. 5. (i) FT-IR spectra of the as-synthesized hectorite-like samples and (ii) Schematic illustration of the bonding structure in clay sheets.

silicate lattice is significantly affected by the distortions of tetrahedral layers [32], it is possible to monitor the structural evolution of the hectorite-like samples with time from the variations of the FT-IR O–H and Si–O vibrations. Generally, these hectorite-like samples contain two strong peaks, which can be attributed to the tetrahedral Si–O stretching and bending vibrations observed at 1010 and 456 cm⁻¹, respectively (Fig. 5 (a)). With increasing synthesis time, the Si–O stretching band centered at 1010 cm⁻¹ becomes narrower due to increased degree of hydration [31-32]. The blue peak shift at 456 cm⁻¹ with hydration time originates from the in-plane bending vibration of Si–O–Si, indicating the enhanced identity of silicon sheets in

specimens with prolonging hydrothermal treatment time [23,33], which is consistent with the results presented in Fig. 4. Furthermore, the intensity of the broad peak centered at 653 cm^{-1} (corresponding to the deformation of OH groups in the H–O–Mg structure) increases with an increase in the hydrothermal treatment time (indicating a more complete rearrangement of the OH groups in the hectorite octahedral lattice [31-35]), while the small and broad absorption peak at around 898 cm^{-1} likely results from the OH bending in the H–O–Si band [24,36-37]. Consequently, due to the assignment of the H–O–Mg and H–O–Si bands in Fig. 5, the Q2 Si structure (which is present in the ^{29}Si spectra depicted in Fig. 4) corresponds to $\text{Si}(\text{OMg})(\text{OSi})_2(\text{OH})$ species.

Figs. 6 and 7 show the FE–SEM and HR–TEM images of the as-synthesized Na hectorites. The inserted SAED patterns mainly exhibit two diffraction rings representing the (130/200) and (330/060) planes, indicating the formation of hectorite-like samples. After increasing treatment time, the number of cracks in the described two-dimensional plates sharply decreases due to the “edge-to-edge” interactions, thus forming Na hectorite nano-plates with high aspect ratios (lateral diameters: $0.7\text{--}5\text{ }\mu\text{m}$, thickness: around 10 nm ; see Fig. 6). In particular, the Hec-264 h sample is characterized by a large aspect ratio of up to 500. In addition, as shown in Figs. 6(c) and (d), the “edges” in these two samples can be attributed to the curled edge view. Furthermore, as shown in Fig. 6, the surfaces of the produced samples contain many uniformly dispersed white dots with sizes ranging from $20\text{ to }200\text{ nm}$. In order to identify these dots, an energy disperse spectroscopy (EDS) technique was

employed. However, the performed EDS mapping and spot analyses were unable to provide detailed information on the main components of these hectorite-like samples (Fig. 6(e)–(i)). Because multiple pores with similar diameters were observed in the TEM image of Hec-96 h (Fig. 7(a)), it can be concluded that the white dots depicted in Fig. 6(b) represent nano-pores. Moreover, after extending the treatment time to 264 h (see Fig. 7(b)), the randomly distributed layered thin lines can be attributed to the scaly cracked and “textured” surfaces containing cross-linked bridges of stacked layers in the nanometer range (15–25 nm).

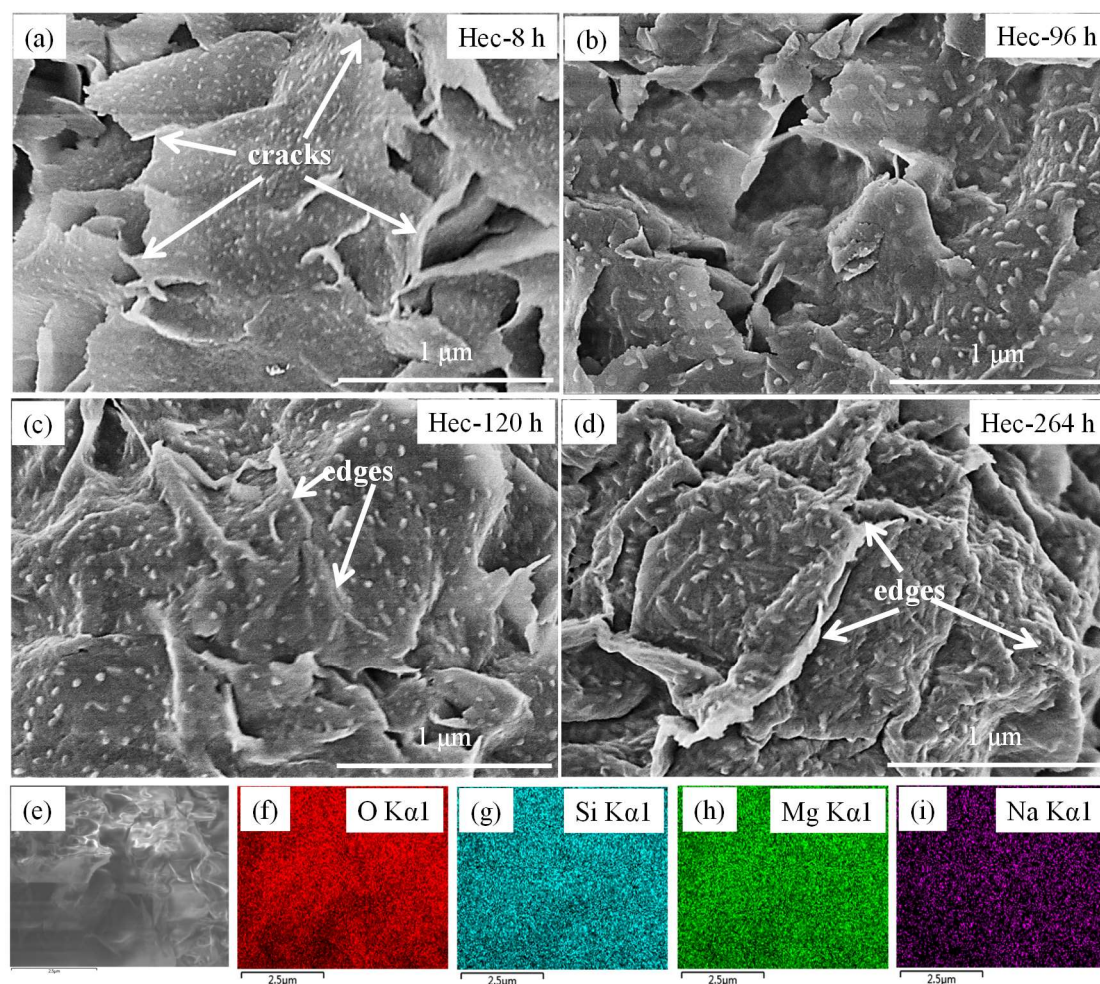


Fig. 6. FE-SEM images of the as-synthesized hectorites produced via the hydrothermal treatment at a temperature of 180°C for (a) 8 h, (b) 96 h, (c) 120 h, and (d) 264 h. (e)–(i) EDS maps obtained for the Hec-8 h sample.

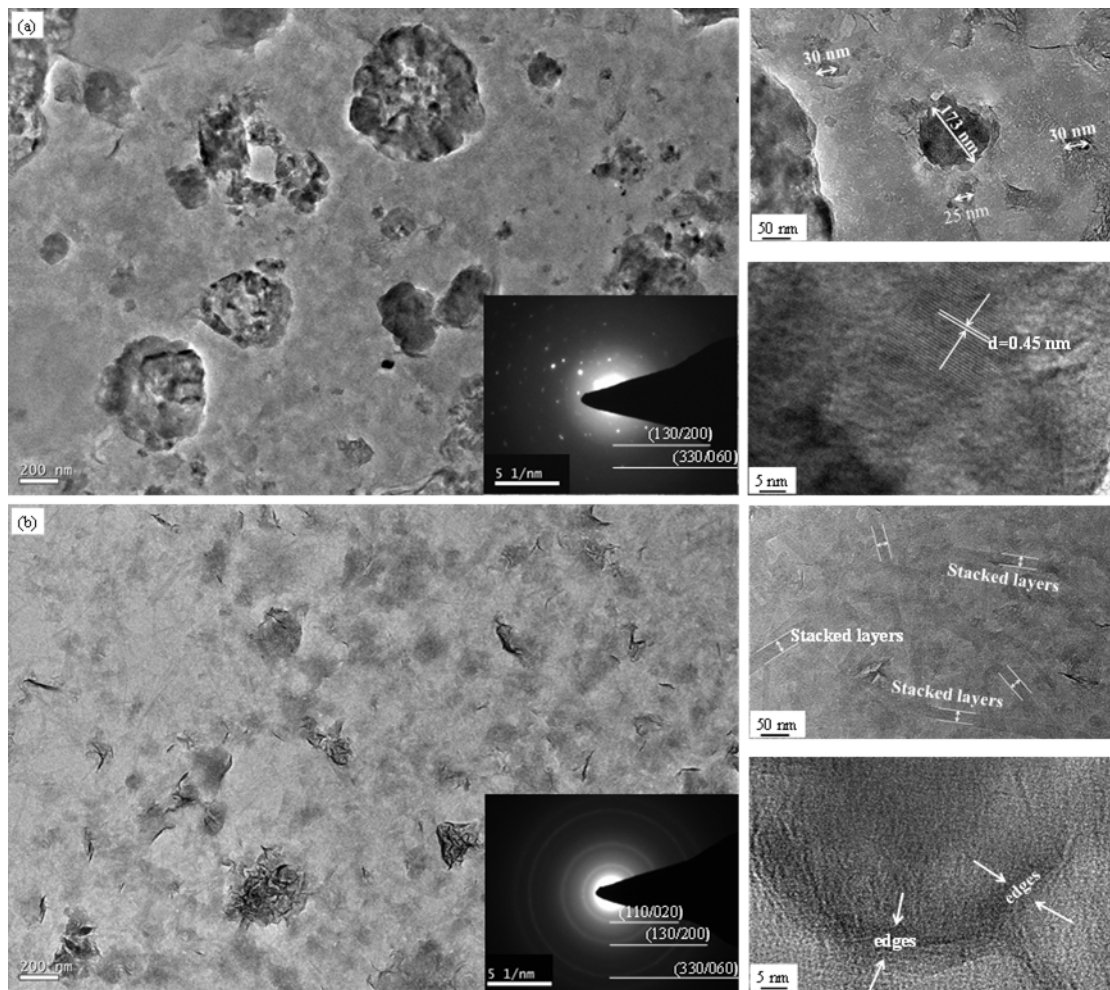


Fig. 7. HR-TEM images of the Na hectorite samples synthesized via the hydrothermal treatment at a temperature of 180°C for (a) 96 h and (b) 264 h. The inserts contain the SAED patterns of the corresponding samples.

Fig. 8 shows the N_2 adsorption-desorption isotherms of the as-synthesized Na hectorites recorded in the relative pressure (P/P_0) range from 10^{-3} to 0.995. According to the IUPAC classification, all the obtained isotherms are similar in shape and correspond to type IV with a typical H_3 hysteresis loops in the P/P_0 range of 0.36–0.95 (which is characteristic of porous plate-like materials). As indicated by the inserted pore size distribution (PSD) graphs depicted in Fig. 8, the average pore size of these samples is about 1.7 nm. In addition, meso-pores and macro-pores are also

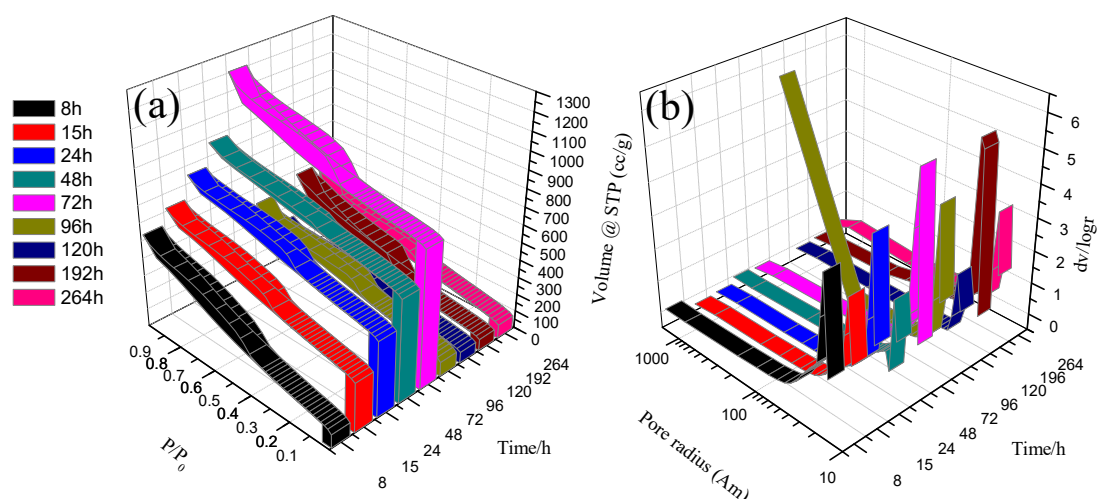


Fig. 8. (a) Nitrogen adsorption-desorption isotherms and (b) PSD desorption graphs of the hectorite clays hydrothermally treated at a temperature of 180°C for different periods.

present in some of the as-prepared specimens, which results in the appearance of hysteresis loops with different shapes [16,38-40]. Moreover, due to the significant reduction in the number of cracks with an increase in the hydrothermal treatment time (Fig. 6), the SSA of the as-prepared samples decreases and becomes stabilized at a level of around 380 m²/g (Table 1). Currently, while some studies reported the mixed appearance of pores with different structures and attempted to establish the effect of the pore structure on SSA, no particular model explaining the relation between them has been proposed [39-41].

The TG/DTA profiles of the synthesized Na hectorite samples are shown in Fig. 9(a). The DTA plot for Hec-8 h exhibits three broad and weak exothermic peaks centered at 60, 374, and 504°C, which can be attributed to the dehydration (60°C) and dehydroxylation (374 and 504°C) of the clay edges and lattice [16]. In contrast, the DTA spectrum recorded for the Hec-264 h sample (DTA-Hec-264 h), contains only two peaks centered at 60 and 480°C corresponding to the dehydration and

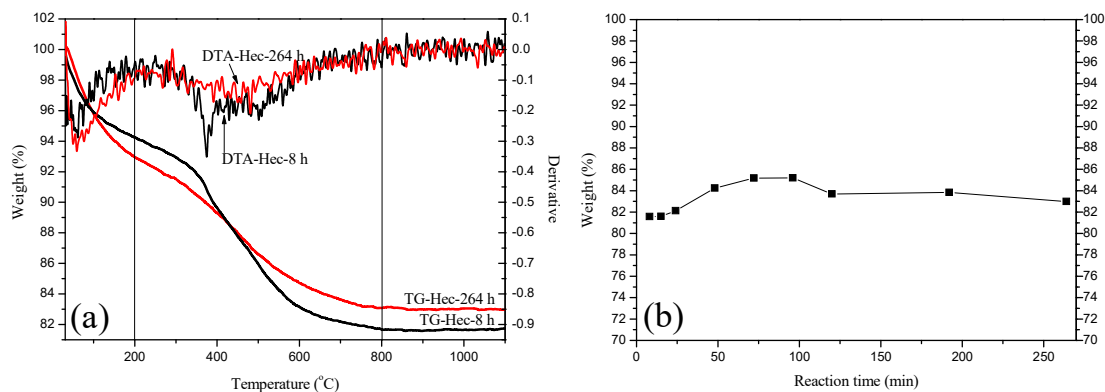


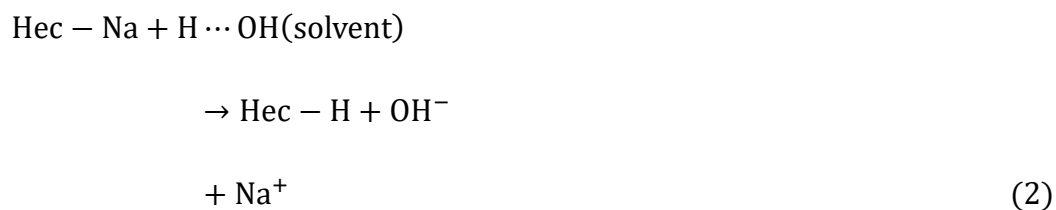
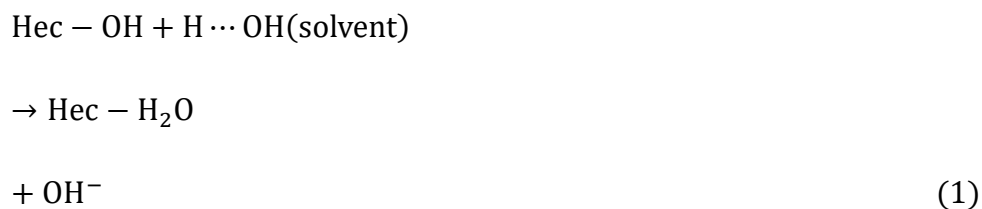
Fig. 9. (a) TG/DTA plots recorded for the Hec-8 h and Hec-264 h samples. (b) Weight variation of the synthetic Na hectorite as a function of the synthesis time.

dehydroxylation processes, respectively. Carrado et al. have demonstrated that the dehydroxylation temperature of hectorites can be as high as 700°C due to their improved crystallinity [16,40], while Dumas et al. reported that the particle size significantly influenced the dehydroxylation temperature of clay talc [19]. However, it was difficult to determine a particular effect produced by the crystallinity and particle size of the Na hectorite samples synthesized in this study since these parameters increased with an increase in the hydrothermal treatments duration. In general, two different mass losses were observed. The first mass loss (30–200°C) resulted from the removal of surface water, and its relative magnitude decreased from 5% to 2% with increasing treatment time due to the relatively small number of water species adsorbed on the particle edges [19]. The second mass loss (200–800°C) originated from the desorption of the edge and interlayer hydroxyl species from the Si and Mg sites. After increasing synthesis time, the resulting Hec-264 h sample exhibited more enhanced crystallinity and textured morphology (as compared to those of the Hec-8 h sample) characterized by a flatter shape of its dehydroxylation plot due to the rapidly

increased particle size and reduced number of defects. The described phenomenon was similar to that observed for synthetic talc powder [19]. As shown in Fig. 9(b), the average total weight fractions of the as-synthesized hectorites were equal to about 83%.

3.2 Electrical conductivity of synthetic Na hectorite dispersions

According to the results presented in Fig. 10(a), the synthesized Na hectorite dispersion exhibit significantly greater electrical conductivities as compared to that of deionized water (around 1 $\mu\text{S}/\text{cm}$; the difference between this measured value and the ideal one (0.05 $\mu\text{S}/\text{cm}$) results from the unavoidable dissolution of CO_2 species from air). Generally, the conductivities of the produced dispersions increase with concentration and synthesis time. Owing to the release of interlayer $\text{Na}^+/\text{Li}^+/\text{NH}_4^+$ cations and protonation of the edge OH groups, the pH of the hectorite-like suspensions is usually higher than 7 [42,43], which can be illustrated by reactions (1)–(2) below.



where Hec–OH denotes the synthetic hectorites containing OH groups, while Hec–Na and Hec–H indicate the synthetic hectorites containing Na⁺ and H⁺ interlayer cations.

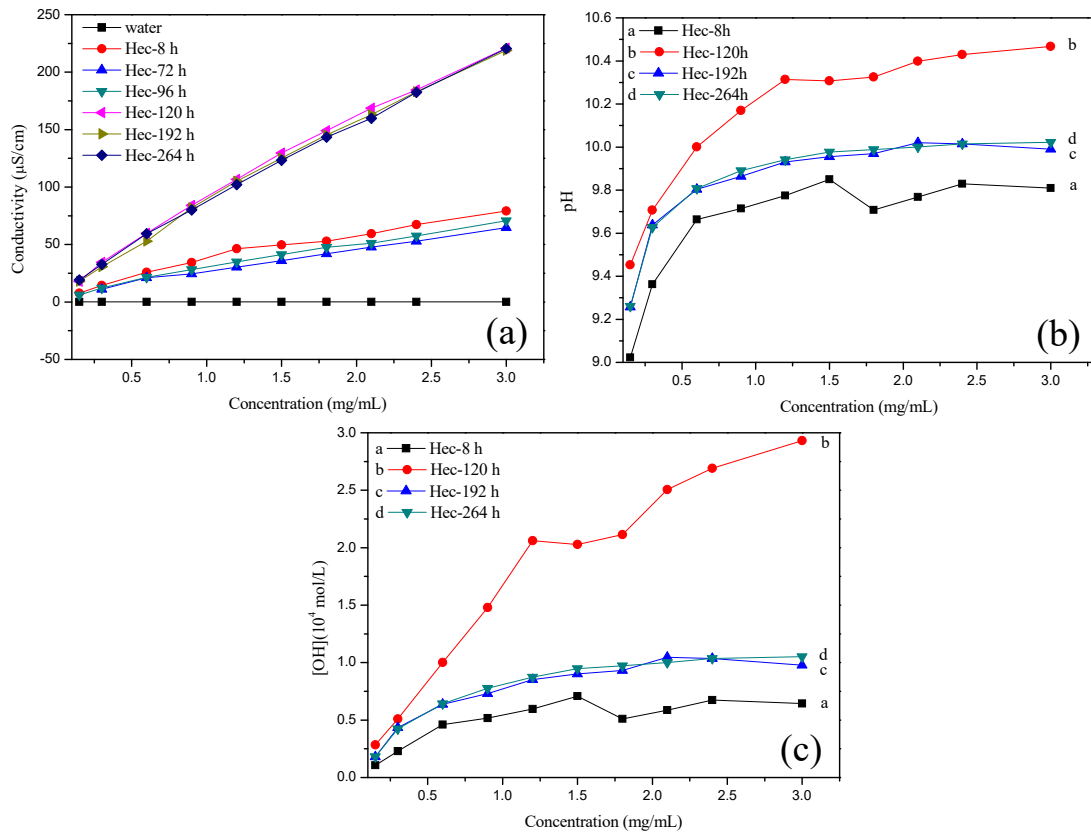


Fig. 10. (a) Electrical conductivity, (b) pH, and (c) calculated OH⁻ anion concentration of the synthetic hectorite dispersions plotted as functions of concentration.

Therefore, the electrical conductivity (σ) of a suspension (which is equivalent to its ion conductivity σ_{ion}) is generally determined by the presence of active Na⁺ and OH⁻ ions according to equation (1):

$$\begin{aligned}\sigma &= \sigma_{ion} \\ &= F(\mu_{OH}[OH^-]) \\ &+ \mu_{Na}[Na^+])\end{aligned}$$

where F is the Faraday constant, and μ_{OH} and μ_{Na} are the mobilities of OH^- and Na^+ ions, respectively. However, the electrical conductivities of the dispersions prepared in this study, are described by more complex relationships.

The conductivities of the Hec-8 h, Hec-15 h, Hec-24 h, Hec-48 h, and Hec-96 h samples mainly depend on the protonation of the OH groups attached to the Si and Mg sites. The Hec-120 h, Hec-192 h, and Hec-264 h suspensions exhibit the highest conductivities with similar values. In particular, both the protonation of OH groups and release of interlayer Na^+ ions in the Hec-120 h dispersion contribute to its rapidly increased conductivity (Figs. 10(b)–(c)). In contrast, although the pH values of the Hec-192 h and Hec-264 h samples are smaller than that of Hec-120 h, their increased basal spacing (see Fig. 2) increases the charge carriers mobility μ in equation (1), thus compensating for the decrease in conductivity induced by the rim protonation process. As a result, the conductivities of these suspensions are comparable to that of Hec-120h (see Fig. 10(a)).

In addition to the described two factors (protonation of OH groups and ion release), the intrinsic conductivity of minerals also affects their electrical conductivity. As demonstrated by Karato et al., the presence of two types of defects in minerals, namely the electron (e' with excess negative charges) and hole (h^\bullet with positive

effective charges) ones, contribute to the electrical conductivity of the studied samples, which can be expressed by equation (2) derived by Ziman and Kittel [44,1]:

$$\sigma = 2e^2 \left(\frac{2\pi kT}{h^2} \right)^{3/2} \times (m_e m_h)^{3/4} \times (\mu_h + \mu_e) \times \exp\left(-\frac{E_g}{2RT}\right) = A \exp\left(-\frac{E_g}{2RT}\right) \quad (2)$$

where e is the elementary charge of electron; k is the Boltzmann constant; R is the gas constant; h is the Plank constant; $m_{e,h}$ is the effective mass of electron or hole respectively; $\mu_{e,h}$ is the mobility of electron or hole, respectively; and E_g is the optical

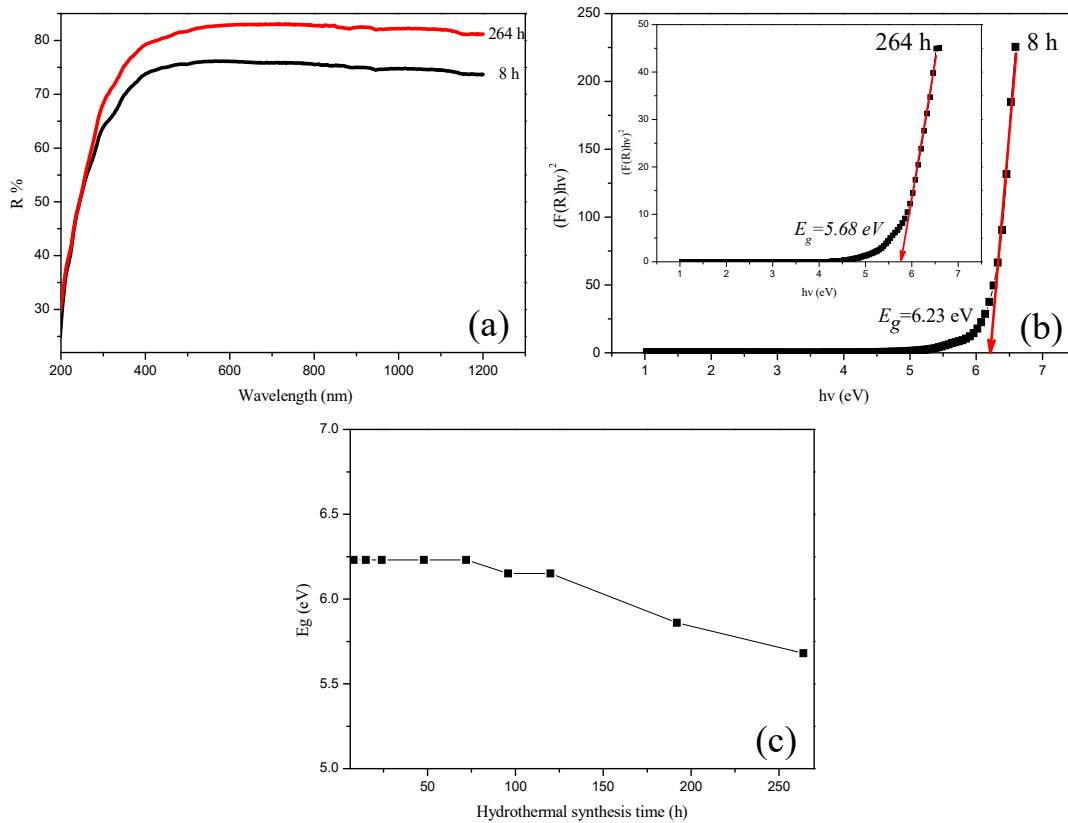


Fig. 11. UV-vis diffuse reflectance spectra, (b) a plot of $(ahv)^2$ vs (hv) for the synthetic hectorites hydrothermally treated at 180 °C for 8 and 264 h, and (c) calculated E_g of the studied samples as a function of the hydrothermal treatment duration.

band gap. Therefore, in order to determine the contribution of intrinsic conductivity to the electrical conductivity of synthetic Na hectorites, it is necessary to investigate the variations of E_g with the hydrothermal treatment duration.

The DRS of the Hec-8 h and Hec-264 h samples recorded in the wavelength region of 200–800 nm are shown in Fig. 11(a). In the range of 290–800 nm, both samples exhibit absorbance values between 16 and 24%. The obtained reflectance spectra were converted to absorbance ones using the Kubelka-Munk equation (3) [45]:

$$F(R) = \frac{(1-R)^2}{2R} = \frac{\alpha}{S}$$

where α is the absorption coefficient, S is the scattering coefficient, and R is the reflectance. Thus, the optical band gap energy (E_g) of hectorites was calculated using equation (4) derived by Mott and Davis [46-47]:

$$(\alpha h\nu)^m = B(h\nu - E_g)$$

where B is the constant independent of the photon energy, $h\nu$ is the photon energy, α is the absorption coefficient, and m is the parameter depending on the type of the photon-induced transition ($m = 1/2$ for the allowed direct transitions and $m = 2$ for the

allowed indirect transitions). Therefore, by combining equation (3) and (4), equation (5) was obtained:

$$(F(R)hv)^m \\ = B(hv \\ - E_g)$$

In this work, the magnitude of E_g was estimated by extrapolating the linear regression of $(F(R)hv)^2$ versus hv to zero. As shown in Fig. 11(b), the linear plots of $(F(R)hv)^2$ vs (hv) obtained for the studied synthetic hectorites indicate that their absorption mechanism corresponds to the allowed indirect transitions [46-47]. The magnitudes of E_g determined for the synthetic Na hectorites treated for 8 and 264 h are 6.23 and 5.68 eV, respectively. The variations of E_g of synthetic Na hectorites plotted as functions of the synthesis time are shown in Fig. 11(c). The obtained results indicate that the increase in the duration of hydrothermal treatment increases the conductivity of synthetic Na hectorites and decreases their E_g . According to equation (2), since the difference between the highest and lowest values of E_g is only around 0.55 eV, the contribution of the intrinsic conductivity of synthetic Na hectorites to their electrical conductivity (which is described by the term $\exp(-\frac{E_g}{2RT})$) is negligible.

4. Conclusions

In this work, we have successfully synthesized Na hectorite nanolayers with

tunable aspect ratios via the hydrothermal method using the Qarhan Salt Lakes brine as a starting material. The obtained results indicate that the prolonged hydrothermal duration contributes to the preferred growth of 2-dimensional synthetic Na hectorites along their (001) plane and to the increased CEC and aspect ratio. After investigating the influences of various factors on the electrical conductivity of the produced hectorites, it was concluded that the observed conductivity variations of synthetic Na hectorite suspensions resulted from the protonation of edge OH groups and release of interlayer cations, and not from their intrinsic conductivity.

Acknowledgements

This work was financially supported by the National Natural Science Foundation of China (grant No. 24101210), Qinghai Science & Technology projects (grant No. 2016-GX-102), Youth Innovation Promotion Association of the Chinese Academy of Sciences (CAS; grant No. 2016376), CAS programs “Light of West China” and “Hundred Talents”, and open project of the State Key Laboratory of Chemical Resource Engineering (grant No. CRE-2017-c-202).

References

- [1] E. Ruiz - Hitzky, Conducting polymers intercalated in layered solids, *Adv. Mater.* 5 (1993) 334–340.
- [2] H.J. Walls, M.W. Riley, R.R. Singhal, R.J. Spontak, P.S. Fedkiw, S.A. Khan, Nanocomposite electrolytes with fumed silica and hectorite clay networks: Passive

- versus active fillers, *Adv. Funct. Mater.* 13 (2003) 710–717.
- [3] R.G. Singhal, M.D. Capracotta, J.D. Martin, S.A. Khan, P.S. Fedkiw, Transport properties of hectorite based nanocomposite single ion conductors, *J. Power Sources* 128 (2004) 247–255.
- [4] S. Cheng, D.M. Smith, Q. Pan, S. Wang, C.Y. Li, Anisotropic ion transport in nanostructured solid polymer electrolyte, *RSC Adv.* 5 (2015) 48793–48810.
- [5] N. Miyamoto, Y. Yamada, S. Koizumi, T. Nakato, Extremely stable photoinduced charge separation in a colloidal system composed of semiconducting niobate and clay nanosheets, *Angew. Chem. Int. Ed.* 46 (2007) 4123–4127.
- [6] J. Liu, G. Zhang, Recent advances in synthesis and applications of clay-based photocatalysts: A review, *Phys. Chem. Chem. Phys.* 16 (2014) 8178–8192.
- [7] M.A. Bizeto, A.L. Shiguihara, V.R.L. Constantino, Layered niobate nanosheets: Building blocks for advanced materials assembly, *J. Mater. Chem.* 19 (2009) 2512–2525.
- [8] T. Sónchez, P. Salagre, Y. Cesteros, Ultrasounds and microwave-assisted synthesis of mesoporous hectorites, *Microporous Mesoporous Mater.* 171 (2013) 24–34.
- [9] J.H. Lee, J.P. Singer, E.L. Thomas, Micro-/nanostructured mechanical metamaterials, *Adv. Mater.* 24 (2012) 4782–4810.
- [10] K. Manna, C. Hsieh, S.C. Lo, Y. Li, H.N. Huang, W.H. Chiang, Graphene and graphene-analogue nanosheets produced by efficient water-assisted liquid exfoliation of layered materials, *Carbon* 105 (2016) 551–555.
- [11] L. Niu, J.N. Coleman, H. Zhang, H. Shin, M. Chhowalla, Z. Zheng, Production

of two-dimensional nanomaterials via liquid-based direct exfoliation, *Small* 12 (2016) 272–293.

[12] H. Kalo, M.W. Möller, D.A. Kunz, J. Brey, How to maximize the aspect ratio of clay nanoplatelets, *Nanoscale* 4 (2012) 5633–5639.

[13] T. Lan, P.D. Kaviratna, T.J. Pinnavaia, Mechanism of clay tactoid exfoliation in epoxy-clay nanocomposites, *Chem. Mater.* 7 (1995) 2144–2150.

[14] I. Vicente, P. Salagre, Y. Cesteros, F. Guirado, F. Medina, J.E. Sueiras, Fast microwave synthesis of hectorite, *Appl. Clay Sci.* 43 (2009) 103–107.

[15] T.D. Burchell, R.R. Judkins, M.R. Rogers, A.M. Williams, A novel process and materials for the separation of carbon dioxide and hydrogen sulfide gas mixtures, *Carbon* 35 (1997) 1279–1294.

[16] K.A. Carrado, R. Csencsits, P. Thiyagarajan, S. Seifert, S.M. Macha, J.S. Harwood, Crystallization and textural porosity of synthetic clay minerals, *J. Mater. Chem.* 12 (2002) 3228–3237.

[17] G. Sandí, H. Joachin, R. Kizilel, S. Seifert, K.A. Carrado, In situ SAXS studies of the structural changes of polymer nanocomposites used in battery applications, *Chem. Mater.* 15 (2003) 838–843.

[18] K.A. Carrado, L. Xu, D.M. Gregory, K. Song, S. Seifert, R.E. Botto, Crystallization of a layered silicate clay as monitored by small-angle X-ray scattering and NMR, *Chem. Mater.* 12 (2000) 3052–3059.

[19] A. Dumas, F. Martin, C.L. Roux, P. Micoud, S. Petit, E. Ferrage, J. Brendlé, O. Grauby, M. Greenhill-Hooper, Phyllosilicate synthesis: A way of accessing edges

contributions in NMR and FT-IR spectroscopies. Example of synthetic talc, *Phys. Chem. Miner.* 40 (2013) 361–373.

[20] M.W. Möller, D. Hirsemann, F. Haarmann, J. Senker, J. Breu, Facile scalable synthesis of rectorites, *Chem. Mater.* 22 (2010) 186–196.

[21] L. Zhuo, J. Ge, L. Cao, B. Tang, Solvothermal synthesis of CoO, Co₃O₄, Ni(OH)₂ and Mg(OH)₂ nanotubes, *Cryst. Growth Des.* 9 (2009) 1–6.

[22] I. Vicente, P. Salagre, Y. Cesteros, Preparation of pure hectorite using microwaves, *Phys. Proc.* 8 (2010) 88–93.

[23] Y. Wang, Q. Wang, Z. Liu, Z. Zhou, S. Li, J. Zhu, R. Zou, Y. Wang, J. Lin, Y. Zhao, Structural manipulation approaches towards enhanced sodium ionic conductivity in Na-rich antiperovskites, *J. Power Sources* 293 (2015) 735–740.

[24] O. Allahdin, M. Wartel, G. Tricot, B. Revel, A. Boughriet, Hydroxylation and dealumination of a metakaolinite-rich brick under acid conditions, and their influences on metal adsorption: One- and two-dimensional (¹H, ²⁷Al, ²³Na, ²⁹Si) MAS NMR, and FTIR studies, *Microporous Mesoporous Mater.* 226 (2016) 360–368.

[25] S.S. Hou, F.I. Beyer, K. Schmidt-Rohr, High-sensitivity multinuclear NMR spectroscopy of a smectite clay and of clay-intercalated polymer, *Solid State Nucl. Magn. Reson.* 22 (2002) 110–127.

[26] S. Lantenois, R. Champallier, J.M. Bény, F. Muller, Hydrothermal synthesis and characterization of dioctahedral smectites: A montmorillonites series, *Appl. Clay Sci.* 38 (2008) 165–178.

[27] D.W. Sindorf, G.E. Maciel, Solid-state NMR studies of the reaction of silica

surfaces with polyfunctional chloromethylsilanes and ethoxymethylsilanes, *J. Am. Chem. Soc.* 105 (1983) 3767–3776.

[28] V.I. Bakhmutov, Strategies for solid-state NMR studies of materials: From diamagnetic to paramagnetic porous solid, *Chem. Rev.* 111 (111) 530–562.

[29] E. Lippmaa, M. Mägi, A. Samoson, G. Engelhardt, A.R. Grimmer, Structural studies of silicate by solid-state high-resolution ^{29}Si NMR, *J. Am. Chem. Soc.* 102 (1980) 4889–4893.

[30] J. Jiao, S.S. Ray, W. Wang, J. Weitkamp, M. Hunger, Effect of dehydration on the local structure of framework silicon atoms in zeolite Y investigated by solid-state NMR spectroscopy, *Z. Anorg. Allg. Chem.* 631 (2005) 484–490.

[31] J. Madejová, J. Bujdák, M. Janek, P. Komadel, Comparative FT-IR study of structural modifications during acid treatment of dioctahedral smectites and hectorite, *Spectrochim. Acta, Part A* 54 (1998) 1397–1406.

[32] L. Yan, C.B. Roth, P.F. Low, Changes in the Si-O vibrations of smectite layers accompanying the sorption of interlayer water, *Langmuir* 12 (1996) 4421–4429.

[33] S. Xie, X. Han, Q. Kuang, Y. Zhao, Z. Xie, L. Zheng, Intense and wavelength-tunable photoluminescence from surface functionalized MgO nanocrystal clusters, *J. Mater. Chem.* 21 (2011) 7263–7268.

[34] J.T. Kloprogge, R.L. Frost, L. Hickey, Infrared emission spectroscopic study of the dehydroxylation of some hectorites, *Thermochim. Acta* 345 (2000) 145–156.

[35] M. Maiti, A.K. Bhowmick, Synthesis and properties of new fluoroelastomer nanocomposites from tailored anionic layered magnesium silicates (hectorites), *J.*

Appl. Polym. Sci. 111 (2008) 1094–1104.

[36] R.A. Levy, L. Chen, J.M. Grow, Y. Yu, A comparative study of plasma enhanced chemically vapor deposited Si-O-H and Si-N-C films using the environmentally benign precursor diethylsilane, Mater. Lett. 54 (2002) 102–107.

[37] T.D. Courtney, C.C. Chang, R.J. Gorte, R.F. Lobo, W. Fan, V. Nikolakis, Effect of water treatment on Sn-BEA zeolite: Origin of 960 cm⁻¹ FTIR peak, Microporous Mesoporous Mater. 210 (2015) 69–76.

[38] G. Sethia, H.A. Patel, R.R. Pawar, H.C. Bajaj, Porous synthetic hectorites for selective adsorption of carbon dioxide over nitrogen, methane, carbon monoxide and oxygen, Appl. Clay Sci. 91–92 (2014) 63–69.

[39] D. Chen, Z. Qu, Y. Sun, Y. Wang, Adsorption-desorption behavior of gaseous formaldehyde on different porous Al₂O₃ materials, Colloids Surf. A 441 (2014) 433–440.

[40] K.A. Carrado, S.M. Macha, D.M. Tiede, Effects of surface functionalization and organo-tailoring of synthetic layer silicates on immobilization of cytochrome c, Chem. Mater. 16 (2004) 2559–2566.

[41] T. Zelenka, Adsorption and desorption of nitrogen at 77 K on micro- and meso-porous materials: Study of transport kinetics, Microporous Mesoporous Mater. 227 (2016) 202–209.

[42] R. Shu, W. Sun, X. Liu, Z. Tong, Temperature dependence of aging kinetics of hectorite clay suspensions, J. Colloid Interface Sci. 444 (2015) 132–140.

[43] A. Cadene, S. Durand-Vidal, P. Turq, J. Brendle, Study of individual

Na-montmorillonite particles size, morphology, and apparent charge, *J. Colloid Interface Sci.* 285 (2005) 719–730.

[44] S. Karato, D. Wang, *Physics and Chemistry of the Deep Earth*. John Wiley & Sons, Ltd., 2013.

[45] R.A. Schoonheydt, UV-VIS-NIR spectroscopy and microscopy of heterogeneous catalysts, *Chem. Soc. Rev.* 39 (2010) 5051–5066.

[46] M. Caglar, Y. Caglar, S. Aksoy, S. Ilican, Temperature dependence of the optical band gap and electrical conductivity of sol-gel derived undoped and Li-doped ZnO films, *Appl. Surf. Sci.* 256 (2010) 4966–4971.

[47] M.M.A. Imran, O.A. Lafi, Electrical conductivity, density of states and optical band gap in $\text{Se}_{90}\text{Te}_6\text{Sn}_4$ glassy semiconductor, *Physica B* 410 (2013) 201–205.